Investigation of mechanisms leading to laser damage morphology

L. Lamaignère[1], M. Chambonneau[1], R. Diaz[1], P. Grua[1], R. Courchinoux[1], J.-Y. Natoli[2] and J.L. Rullier[1]

[1] *CEA, CESTA, F-33116 Le Barp, France*
[2] *Aix-Marseille Université, CNRS, Centrale Marseille, Institut Fresnel UMR 7249, 13013 Marseille, France*

Abstract:

The original damage ring pattern at the exit surface of fused silica induced by highly modulated nanosecond infrared laser pulses demonstrates the time dependence of damage morphology. Such a damage structure is used to study the dynamics of the plasma issued from open cracks. This pattern originates from electron avalanche in this plasma, which simultaneously leads to an ionization front displacement in air and a silica ablation process. Experiments have shown that the propagation speed of the detonation wave reaches about 20 km/s and scales as the cube root of the laser intensity, in good agreement with theoretical hydrodynamics modeling.

During this presentation, we present the different phases and the associated mechanisms leading to this peculiar morphology:

- During an incubation phase, a precursor defect provides energy deposit that drives the near surface material into a plasma state.
- Next the silica plasma provides free electrons in the surrounding air, under laser irradiation an electron avalanche is initiated and generates a breakdown wave.
- Then this breakdown wave leads to an expansion of the air plasma. This latter is able to heat strongly the silica surface as well as generate free electrons in its conduction band. Hence, the silica becomes activated along the breakdown wave.
- When the silica has become absorbent, an ablation mechanism of silica occurs, simultaneously with the air plasma expansion, resulting in the formation of the ring patterns in the case of these modulated laser pulses.

These mechanisms are supported by experiments realized in vacuum environment. A model describing the expansion of the heated area by thermal conduction due to plasma free electrons is then presented.

Next, the paper deals with the two damage formation phases that are distinguished. The first phase corresponds to the incubation of the laser flux by a subsurface defect until the damage occurrence: an incubation fluence corresponds to this phase. The second is related to the damage expansion that only refers to the energy deposit feeding the activation mechanism up to the end of the pulse: an expansion fluence corresponds to this phase. A striking feature is that the damage diameters are proportional to the fluence of expansion at a given shot fluence. Indirectly, the fluences of incubation by the precursors are then determined.

I. INTRODUCTION

Laser applications most often use sources with an injection seeder selecting one single longitudinal mode (SLM) of laser pulses. In the case of SLM, because of the repeatability of the temporal profile, reproducible laser experiments are possible [1,2]. For multiple longitudinal mode (MLM) laser pulses, the temporal instability related to the MLM configuration raise many issues on laser-induced damage (LID) [2-6]. Recent investigations of LID density and damage morphology on exit surface of silica exhibit strong differences between SLM and MLM regimes [7]. At 1064 nm in nanosecond regime, circular ring patterns are observed on the output surface

Laser-Induced Damage in Optical Materials 2016, edited by Gregory J. Exarhos, Vitaly E. Gruzdev,
Joseph A. Menapace, Detlev Ristau, MJ Soileau, Proc. of SPIE Vol. 10014, 1001413
· doi: 10.1117/12.2244827

of silica [7,8]: the ring morphology is due to the formation of an ionization front in surrounding air [7]. To go further in such hypothesis complementary experiments have been performed. For this purpose, the impact of fluence is first investigated and next specific experiments are carried out at different angles of incidence. By varying the fluence, it is shown that the plasma appearance instant (t_0) is not directly correlated with this laser parameter but mainly linked to the disparity of damage precursors present in subsurface of silica material. However, the energy deposit beyond t_0 can be related to the pattern size. Then, in order to confirm the main role of the plasma on the ring pattern formation, the angle of incidence with respect to the component surface is varied. The complete set of experimental works confronted to theoretical considerations confirm that LID morphology at 1064 nm results from surface plasma dynamics. To go further in damage comprehension, additional studies with MLM laser pulses have been performed in vacuum, where the damage morphology is expected to be significantly different.

II. LASER FLUENCE IMPACT ON DAMAGE INITIATION AND SIZE

Experimental studies have been performed on 10 mm thick fused silica samples. Each damage site was initiated in ambient air by one single laser pulse at 1064 nm. The laser facility detailed in Ref. 1 was used to irradiate the samples; it was operated in MLM regimes. At the focus region, the beam spot is Gaussian-shaped and the diameter at 1/e is around 1.5 mm. Fluences available on this facility may reach 130 J/cm². In the present study, the intensity profiles of each pulse have been recorded by means of a 25 GHz bandwidth photo-diode and a 33 GHz bandwidth oscilloscope from Tektronix (DSA73304D). A typical temporal profile is shown in Fig. 1. Note that each acquisition exhibits strong intensity modulations that differ from pulse to pulse. The images of the damage sites are acquired post mortem thanks to Nomarski microscopy.

A systematic analysis of damage morphology versus fluence reveals the presence of multi-pits in the case of fluences > 120 J/cm². An example of such observation is shown in Fig. 1 for 130 J/cm² where two pits have been induced the irradiation. It must be noted that the 200 µm distance between the two pit centers represent less than 10% in fluence variation (because of the spot size). This weak difference in fluence cannot explain the differences between the two damage sizes and morphologies. As it has been proposed and detailed in Ref. 6, we match intensity spikes with the rings. The Fig. 1 shows the same intensity profile associated with the two ring patterns. For each site, the times t_0 (red arrow) correspond to the surface plasma beginning at the center of the respective ring patterns. By considering this ionization starting time we can deduce that the smallest damage site (left part in Fig. 1) has appeared after the largest one (right part in Fig. 1). We thus deduce that this difference in damage size is obviously explained by the different temporal origin (t_0) of plasma creation in air: the sooner the silica surface is activated, the larger the ring pattern will be. The good correlation obtained between a unique temporal profile and several ring patterns supports the scenario previously proposed.[6]

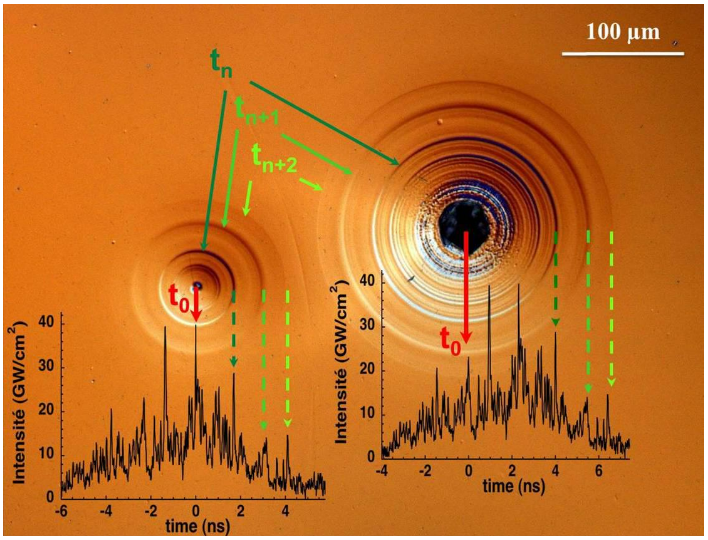

Fig. 1. Correlation of morphology and intensity profile in the case of multi-pits damage initiated by a single laser pulse; the beam diameter is larger than the image.

In order to highlight the role of fluence on damage initiation, we define in Fig. 2 two size limits of damage as SD (Smallest Damage) and LD (Largest Damage). SD is relative to late t_0 (later than t_0 associated to the left pit in Fig. 1), and by opposition, LD corresponds to early t_0 (before than t_0 associated to the right pit in Fig. 1). Thus LD can be associated to very absorbent initiator defects able to produce the most rapidly a plasma. A statistical study has been realized and indicates an increase in the laser damage probability P_{dom} with fluence as already measured for MLM-LID tests [9-11]. However, Nomarski micrographs in Fig. 2 clearly show that there is no direct correlation between fluences and damage sizes.

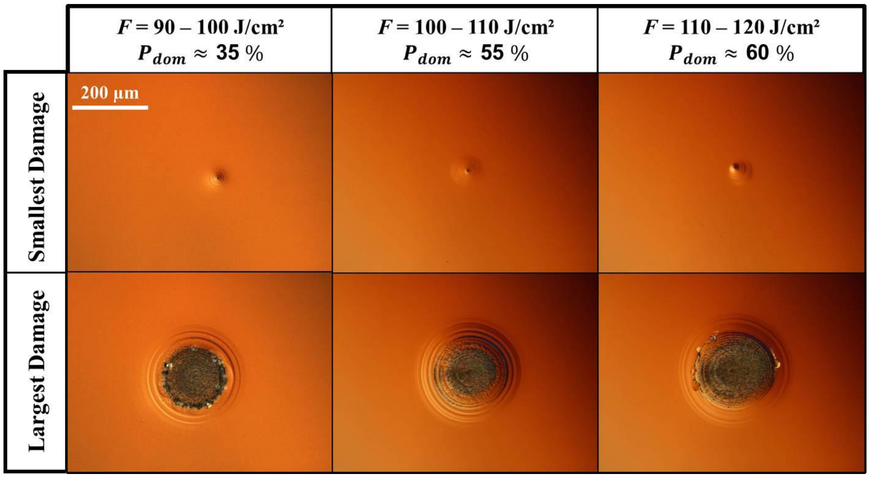

Fig. 2. Smallest (SD) and largest (LD) damage sites for different fluence ranges. Damage probability P_{dom} is indicated for each fluence range.

Further analyses have been specifically carried out on ten distinct LID sites initiated at fluences ranging from 75 to 110 J/cm². On each of these sites, the diameter is reported in Fig. 3 as a function of the total fluence of the corresponding laser pulses (red circles). These results emphasize that there is no correlation between the size of a damage site and the total fluence of the pulse that initiated it, in good agreement with above observations. Previous works realized with silica samples containing absorbent nano-particles have established that, for a given fluence, precursors parameters (absorptivity, size, depth) and the damage size are correlated.[9,10] It has also been found that in the case of gold nano-precursor defect, during a period of incubation the precursor develops, and once a sharp damage threshold is crossed, the transformed silica surface strongly absorbs and releases copious material.[11] In our study, this threshold corresponds to t_0 and the systematic observation that the damage size is not correlated with the total fluence demonstrates that a random aspect of each precursor characteristics drives the damage incubation.

The ionization starting time t_0 that has been determined for each of these sites makes possible to separate the two damage formation phases. The first phase corresponds to the absorption of the laser flux by a subsurface precursor defect until t_0. Then the second phase is related to the damage expansion due to the ionization front displacement simultaneously with ablation processes up to the end of the pulse. Thereby, the total fluence F_{tot} of a laser pulse can be written as:

$$F_{tot} = F_{abs} + F_{exp} = \int_{-\infty}^{t_0} I(t')dt' + \int_{t_0}^{+\infty} I(t')dt', \quad \textbf{(1)}$$

where I is the laser intensity, F_{abs} and F_{exp} are relative to the absorption by the precursor defect and damage expansion, respectively. Then for each damage site we associate its diameter with the corresponding F_{exp}. At t_0, where $F_{exp} = 0$, the expansion is not yet effective and then the damage diameter is zero. For the ten damage sites the diameter as a function of expansion fluence is reported in Fig. 3 (black diamonds). The damage diameters increase linearly with F_{exp} and, as required, verifies that $\emptyset = 0$ for $F_{exp} = 0$. Despite previous work have mentioned a strong damage size increase with fluence,[8] here we state that this increase is effective only considering F_{exp} and not F_{tot}. Moreover thanks to the precise knowledge of t_0, a linear behavior is revealed.

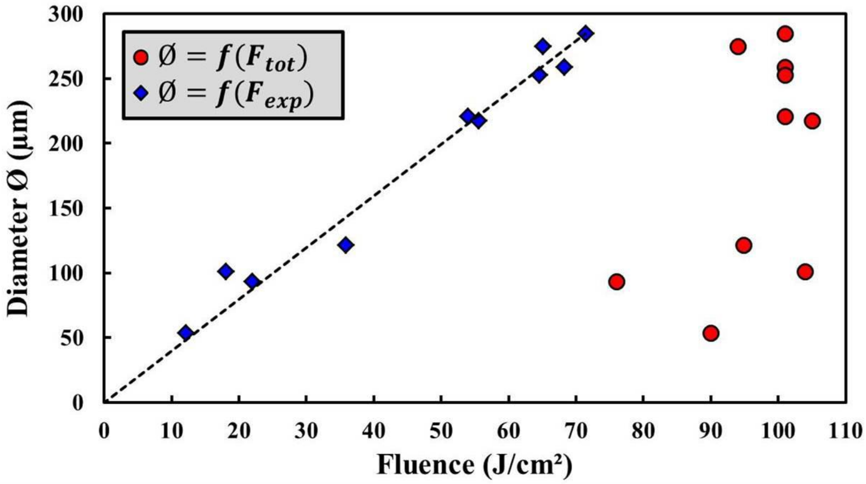

Fig. 3. Damage diameter as a function of: the total fluence (red circles) and the expansion fluence (blue squares).

III. BEAM INCIDENCE EFFECT ON DAMAGE MORPHOLOGY

For infrared irradiation the exit surface damage morphology results from a coupling between the plasma emitted by a subsurface defect and ambient air [12,13]. Notably, in the case of temporally modulated pulses, damage sites show a ring pattern that is closely associated with intensity spikes, thereby making possible the evaluation of plasma expansion speed. To confirm this approach we have varied in our experiments the angle of incidence (noted θ) between the laser beam and the sample, to break the axial symmetry of the pattern. The reflected part of the laser flux on the entrance surface as well as the increase in the beam spot size due to the angle θ have been taken into account while evaluating the laser fluence on the exit surface of the sample.

An example of pattern obtained for $\theta = 40°$ at 95 J/cm² is displayed in Fig. 4(a). We observe in this case that the ring pattern becomes egg-shaped. The major axis appears to be stretched upstream the laser beam and contracted in the opposite direction. In this configuration, we define three different ring appearance speeds related to the different directions as indicated in Fig. 4(a). The speed V is associated to the minor axis and speeds $V^{+/-}$ to the major axis. The three areas corresponding to these different speeds are reported in Fig. 4(b), where the pattern has been rescaled in order to adjust V^+ and V^- to V. These rescalings of V^+ and V^- clearly shows a good fit with V (along the dashed circles), highlighting coefficients of stretching and compression noted C^+ and C^-, respectively.

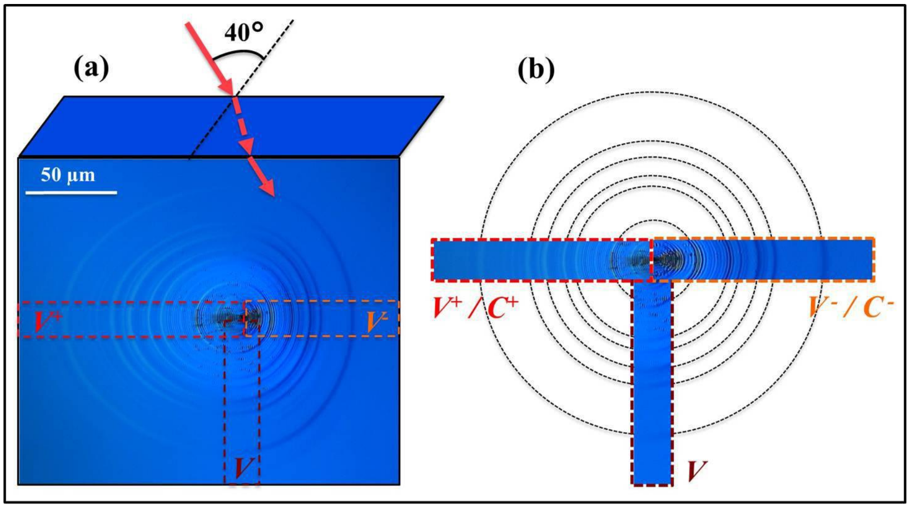

Fig. 4. (a) Nomarski image of a damage after irradiation at $\theta = 40°$ from the normal. (b) Adjustment of the two speeds V^+ and V^-, associated with the laser direction, and the perpendicular speed V.

Thanks to a model based on hydrodynamics where the ionization front speed is proportional to the cube root of laser intensity, we have fitted correctly the measured plasma speed.[6] By introducing I_0, a constant intensity representative of our experiments (set to 10 GW/cm²), we have obtained the relation:

$$V = V_0 \left(\frac{I}{I_0}\right)^{\frac{1}{3}}, \tag{2}$$

where I is the laser intensity and V_0 is a fitting parameter having the dimension of a speed. In this study, measurements have shown that V (along the minor axis) is independent of the angle of incidence. We have extracted the ionization front speed V_0 in all the experimental configurations. An average V_0 value of 20 km/s has been obtained at all angles.

In order to quantify the coefficients C^+ and C^- as a function of the angle of incidence we have used several damage sites initiated for θ values ranging from 0 to 80°. In Fig. 5, the evolution of the ring patterns is reported for eight θ values. We observe that the deformation of rings becomes more pronounced, when the angle of incidence is increased. On the basis of the method shown in Fig. 4, the coefficients C^+ and C^- have been deduced. Their evolutions displayed in Fig. 6 are related to the increase or decrease of the ionization front speed which is directly linked to the incidence angle. One can observe that the decrease in C^- is weak compared to the increase in C^+. When the ionization front displacement and the laser beam are closely in the opposite directions (80°), the ionization front speed is the highest leading to $C^+ = 2.40 \pm 0.15$.

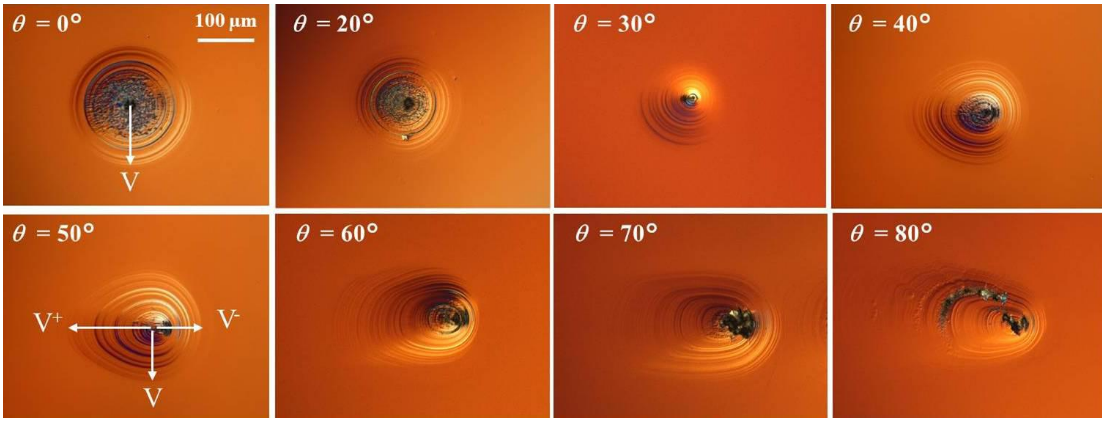

Fig. 5. Nomarski images of damage morphology for different laser beam angle of incidence ranging from 0 to 80°.

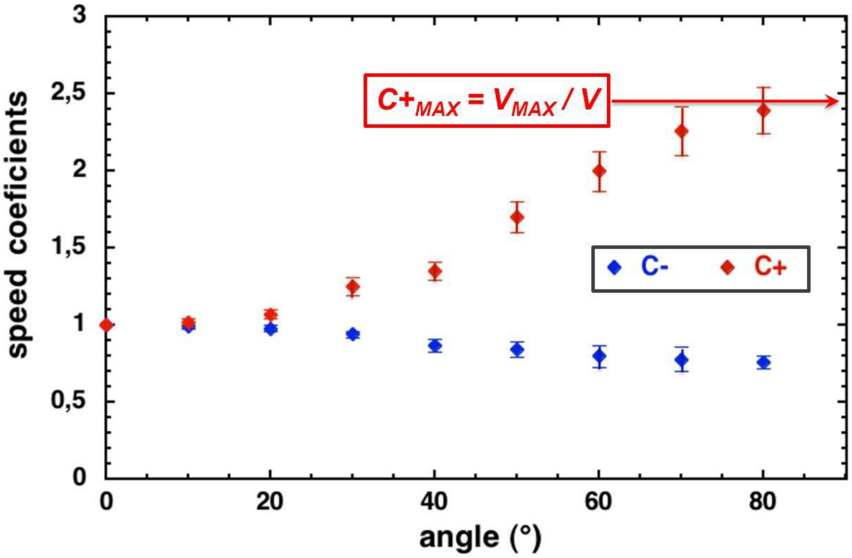

Fig. 6. Evolution of maximum and minimum speed coefficients as a function of the irradiation angle. The dashed arrow indicates the upper limit of C+. The error bars represent the standard deviation.

We propose a possible explanation of the egg-shaped pattern based on the plasma illumination regarding the incident beam. The expanding plasma activates the silica surface. Then the plasma absorbs the laser which is not screened by the hot silica. At the same time the absorbent silica under the surface of the crater is vaporized and thus dig and enlarge the crater during the next pulse, creating a new ring. From the hot silica, an absorption front moves upstream the laser flux, leading to an ablation process similar to mechanisms involved in the technique of laser backside etching [14].

This complementary study by varying the incidence angle of the laser confirms the hypothesis of a surface plasma driven by the laser from t_0 until the end of the pulse. In the case of $\theta = 90°$, an upper limit of the ionization front speed can be evaluated according to the equation:

$$V_{max} = \left[2(\gamma^2 - 1)\frac{I}{\rho_0}\right]^{\frac{1}{3}}, \tag{3}$$

where γ = 1.33 is the ratio of specific heats of the air and ρ_0 = 1.3 kg/m^3 its initial density. With I_0 = 10 GW/cm² and V_0 = 20 km/s previously established, from equations (1) and (2), we evaluate a maximum coefficient:

$$C^{+}_{MAX} = V_{max}/V = 2.45.$$

This upper limit is consistent with the result reported in Fig. 6, where C^{+}=2.40 at θ = 80°.

IV EXPERIMENTAL INVESTIGATIONS OF THE INFLUENCE OF VACUUM ON LID MORPHOLOGIES

The set-up described in ref. [9] is used at 1064 nm both in Single Longitudinal Mode (SLM) and MLM regimes to perform this study in vacuum environment. In the SLM regime, the pulse equivalent duration, defined as the ratio of the energy over the peak power, is 9 ns. The sample is positioned in the focal plane where the spot is Gaussian-shaped and 1 mm in diameter at 1/e. The Rayleigh range of the beam is much longer than the sample thickness. Therefore, the intensity profiles are recorded for each laser shot with a 25 GHz bandwidth photodiode and a 33 GHz bandwidth oscilloscope (Tektronix DSA73304D). Experiments are performed on fused silica samples of 10 mm thickness that exhibit plane super-polished surfaces. The samples are used as a window for the vacuum chamber in which the test will be performed. The front surface is in air environment whereas the rear surface is in vacuum environment. A turbo-molecular pump permits to reach a pressure level of 10^{-5} mbar. Each damage site was initiated by a single laser pulse at 1064 nm. Since the beam is collimated during the propagation in the sample, LID systematically occurs on the rear surface. For both SLM and MLM regimes, the largest damage sites show very similar sizes despite strongly different morphologies. Nomarski Interference Contrast (NIC) micrographs of these damage sites obtained in vacuum are shown in Fig. 7, together with equivalent damage achieved in air environment. The fluences of the shots that initiated the damage sites are 110 J/cm² in all cases. In both SLM and MLM configurations, the damage sizes are reduced by more than a factor of two once the surrounding air is removed. Thus, the scales are multiplied by a factor of two between the images in air and in vacuum. These observations suggest that the environment strongly influences the damage expansion speed. Moreover, the presence of a ring pattern is again systematically obtained in the MLM configuration in vacuum environment.

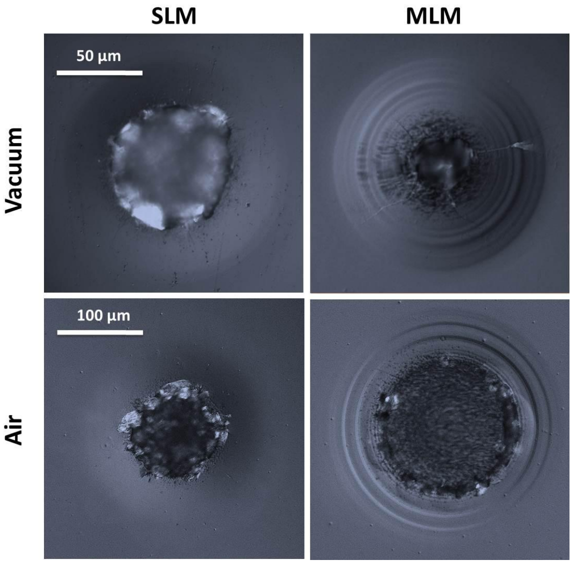

Fig. 7. NIC images of typical damage sites obtained in air and vacuum environments for both SLM and MLM configurations. The fluence of the four shots is 110 J/cm². The scale of the images in vacuum is twice smaller than the scale of the images in air.

Each ring pattern observed on damage sites in the case of MLM pulses is closely associated with intensity spikes. As in air environment, space and time scales are matched, making possible the evaluation of ring appearance speed. In Fig. **8**, a damage site obtained in vacuum environment is shown with the associated intensity profile of the MLM pulse. The white dashed arrows exhibit the correspondence between spikes and rings showing that inner rings appear before outer ones. The red arrow indicates the time t_0 (set to zero on the time scale), associated to the beginning of the formation of the rings. The time t_0 is unique by definition and cannot be shifted to another peak. The stretching as well as the matching of the temporal profile with the rings is also unique. This matching allows us to precisely define the instantaneous ring appearance speed as the ratio of the distance between two successive rings to the time interval separating the two adjacent temporal spikes. Although most intensity spikes can be matched with rings, some dispersion in speed measurement is observed, meaning that ring appearance speed is not constant throughout the pulse. For each speed measurement, we calculate the short-time-average intensity which corresponds to the averaged intensity over the time between the two adjacent spikes (e.g. white dashed arrows in Fig. 8) used to calculate the ring appearance speed.

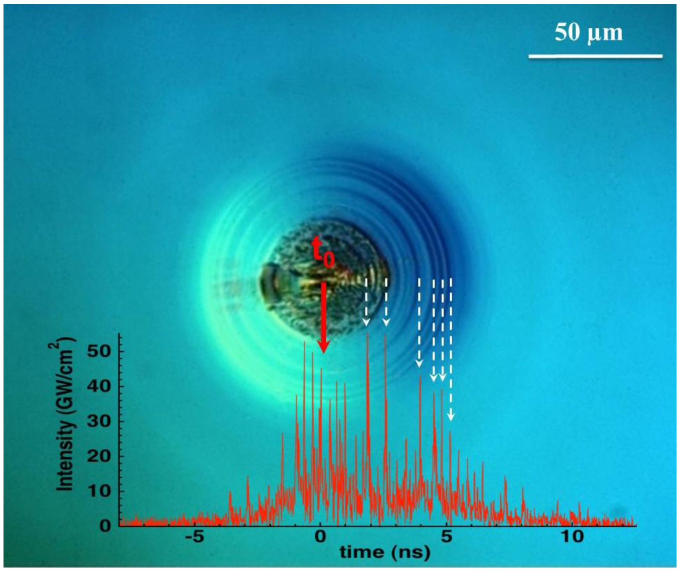

Fig. 8. Correlation between the morphology of a damage site initiated at the rear surface of a fused silica sample in vacuum and the temporal profile of the corresponding MLM pulse.

As an example, we have reported in Fig. 9 the ring appearance speed V as a function of short-time-average laser intensity $\langle I \rangle$ for three damage sites. The three sites in Fig. 9 show very similar results. In order to fit the experimental data a power law $V = a\langle I \rangle^b$ is proposed, where a and b are fitting parameters. This choice makes possible to impose $V = 0$ for $\langle I \rangle = 0$. Similar measurements have been carried out on twelve distinct damage sites initiated in vacuum by different MLM pulses and the mean ring appearance speed reads:

$$V[\mathrm{km/s}] = 2.75\langle I[\mathrm{GW/cm^2}] \rangle^{\frac{1}{2}}. \quad \textbf{(4)}$$

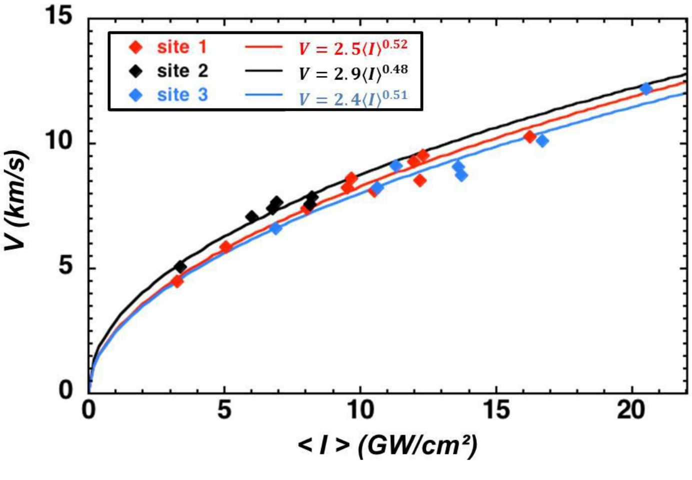

Fig. 9. Instantaneous ring appearance speed as a function of short-time-average laser intensity for three sites initiated in vacuum by three different MLM pulses. The curves stand for the fits of corresponding data.

The ring appearance speed reaches up to 12 km/s. This value is greater than the speed of sound in fused silica (5.9 km/s). The assumed mechanism responsible for the ring pattern formation is linked to the development of a plasma generated by subsurface defects in fused silica and ejected towards vacuum. Classical hydrodynamic processes involved in interaction of lasers with solid materials at intensity levels corresponding to our experiments do not yield such speed values. When air is present, it brings an auxiliary medium able to support plasma expansion speeds in the relevant range. In vacuum, a particular configuration is likely implicated in the generation of a plasma at the vicinity of the surface, which is supposed to be "crawling" on the surface of the sample. In order to illustrate this point, we have tested a specific sample of 10 mm thickness which exit surface is an optical grating, made of periodical pillars of 710 nm height and 140 nm width with a regular spacing of 410 nm. The Rayleigh range is always much larger than the sample thickness. This vertical periodical structure is supposed to inhibit the expansion of the "crawling" plasma along the surface.

For every experiments performed on samples showing a plane exit surface, a systematic ring-pattern is obtained on damage sites (like Fig. **10**(a)), whereas a more fractured damage site without rings is always obtained on the exit surface of the optical grating, as shown in Fig. **10**(b). Thus, a major difference of morphology is observed between the damage sites initiated on the optical grating and the plane surface. Several shots at different fluences were performed on each sample and these observations are independent of the laser fluence. The imprinting of the rings in vacuum never takes place on the surface of the optical grating. In this case, the periodical structure at the surface manifestly prevents the expansion of the "crawling plasma", as assumed earlier.

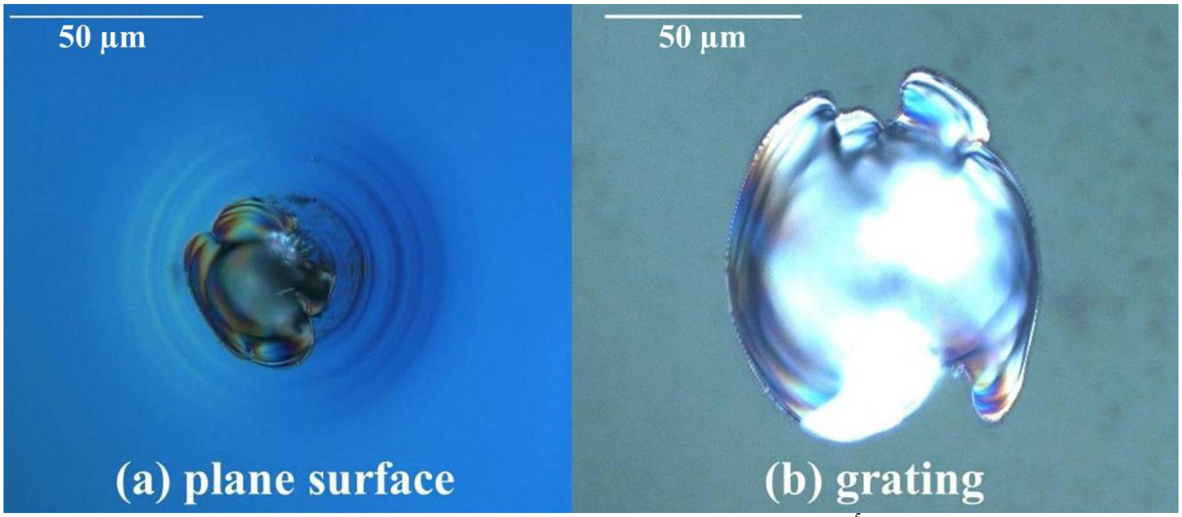

Fig. 10. NIC images of damage sites initiated with MLM pulses in vacuum environment at 10^{-5} mbar on the plane surface (a) and on the optical grating (b) for fluences of 65 J/cm² and 55 J/cm² respectively.

In order to make sure the periodical structure is responsible for the inhibition of the "crawling plasma" expansion in vacuum, additional experiments are performed in air to verify that the formation of a ring pattern still takes place. Thus, the damage sites initiated in air on the surface of the optical grating are compared to those obtained in air on the plane surface. The NIC image of a typical damage sites initiated in air on the exit surface of the optical grating is presented in Fig. 11 with the temporal profiles of the MLM pulse that initiated it. In order to verify that the ring appearance speed of a damage site follows the same law on both surfaces in air environment, the ring formation starting time t_0 and the matching of the rings with intensity spikes have been determined for the damage site of Fig. 11 Then, the instantaneous ring appearance speeds V is supposed to follow the same power law in the ring patterns initiated in air expressed according to:

$$V[\mathrm{km/s}] = 9.3(I[\mathrm{GW/cm^2}])^{\frac{1}{3}}.$$

This assumption is directly confronted to the NIC image as we have expressed the laser intensity as a function of the distance for the MLM pulse that initiated the damage sites in Fig. 11. This distance is written $r(t) = \int_{t_0}^{t} V(\tau)d\tau$, where the speed $V(\tau)$ is taken from the previous relation. Thus, we are able to construct an intensity profile depending on r to be confronted to the NIC image. The good correlation between intensity spikes and the corresponding rings obviously suggests that in air environment, the phase of expansion leading to the formation of the ring patterns neither depends neither on the sample surface state nor on the type of precursor defect involved, provided a plasma is generated. As a consequence, the change in morphologies obtained in vacuum between the damage sites initiated on the plane surface and those obtained on the optical grating can be attributed to the influence of the pillars on the expansion of the "crawling plasma".

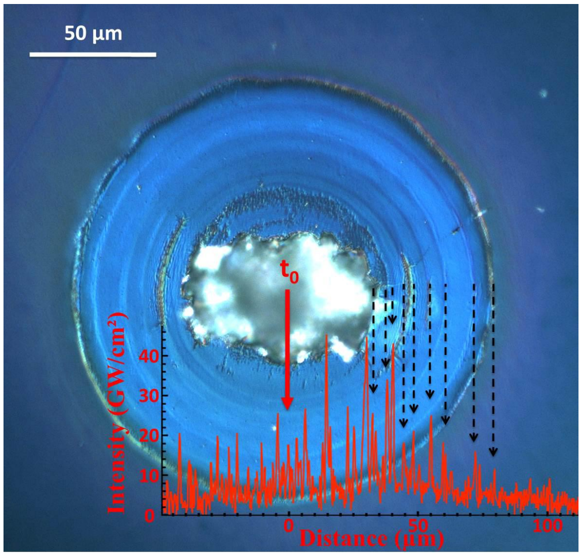

Fig. 11. Damage site initiated in air environment with a single MLM pulse at the surface of the fused silica optical grating. The correspondences between ring patterns and intensity profiles as functions of the distance (in red) are shown. The time t_0 corresponds to the creation of the surface plasma at the center of the damage site (red arrow); black dashed arrows indicate the spike-ring associations.

The hypothesis that a "crawling plasma" could be responsible for the activation of material in vacuum environment, and thus for the imprint of the ring patterns, has been strongly reinforced by experiments involving gratings on the exit surface of optical components. Indeed, in this case, the morphology of the damage sites is completely different from the ones observed on a regular surface and does not show any ring pattern in vacuum. Moreover, when ring patterns are obtained on the plane surface in both environments, measurements have shown different scalings of the speed V with respect to laser intensity: $V \propto I^{1/3}$ for experiments conducted in air and $V \propto I^{1/2}$ in vacuum. The behavior observed in air was attributed to the displacement of an ionization front in the surrounding gas, and a simple hydrodynamic model including the perfect gas approximation has given consistent results for both qualitative and quantitative points of view.

A similar hydrodynamic process, inducing an ionization front propagating within the solid material, may occur in experiments performed in vacuum environment. It can be shown that a $V \propto I^{1/2}$ scaling is obtained in fused silica with the appropriate choice of equation of state of this material, mainly built on the basis of potential energy and elastic pressure contributions. However, although the dependency of speed with respect to laser intensity qualitatively corresponds to experiments, the quantitative results given by this kind of hydrodynamic model for the dense material are out of experimental range (typically lower than 2 km/s). Thus, this is not consistent with the experimental results. Therefore, any hydrodynamic process occurring in the dense material is not considered here.

In that matter, the expansion processes of a high temperature region around the point of damage initiation involving the speeding up of the material must be ruled out. Another mechanism involving the free electrons of the plasma issued from silica expanding towards vacuum can be envisaged. These free electrons may participate in the activation of the material surface by thermal conduction. It is this assumption, which will be retained and the corresponding mechanism of silica surface activation is schematically described in Fig. 12 in which the time is frozen. Three different zones are distinguished to describe the mechanisms responsible for the ring pattern formation. In zone 1, the exit surface is transparent because it has not yet been activated by hot electrons. Zone 2 corresponds to the boundary of the plasma domain. It refers to the propagation of the activation front with the speed V_a. In this zone hot electrons impacting silica surface are able to activate the material, making it absorbent (green arrows). We note that the activated silica surface extends beyond the plasma zone (orange towards green area in silica). The zone which becomes absorbent follows a lateral expansion due to electron heat conduction. In addition the plasma is kept hot due to the laser irradiation (variable dashed red lines), and also fed by the initial surface emission (black arrows). In zone 3, the silica surface is heated and an absorption front moves upstream the laser flux (orange area), deeply inside the material, leading to an ablation process (black arrows) similar to mechanisms involved in the technique of laser backside etching. Each intensity spike illuminating the absorbent surface will then contribute to ablate the material and form a ring pattern, since the absorption front can start from silica surface only once it has been activated by hot electrons.

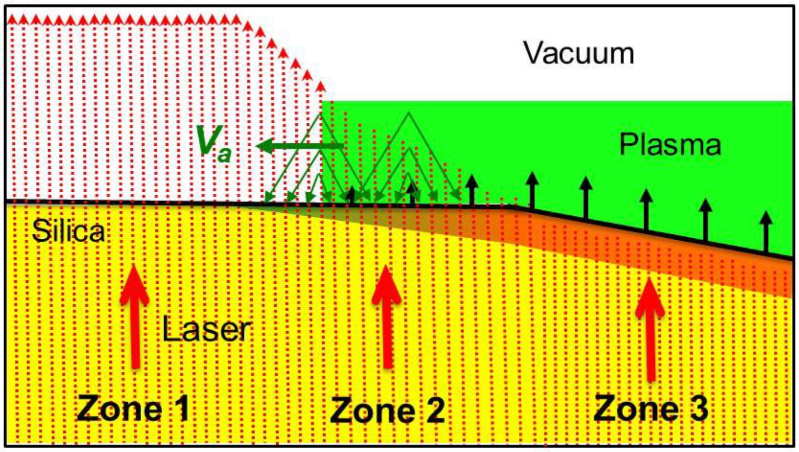

Fig. 12. Schematic illustration of a ring pattern forming for silica interfacing with vacuum.

The mechanisms described above can only take place when the laser flux is high enough to produce an electron avalanche in the medium that expands in vacuum, leading to the creation of a strongly ionized plasma. As reported in Ref. (16), when the ionization degree is still low, the energy level of prime electrons cannot exceed the following value, depending on the laser wavelength λ and on the laser intensity I:

$$E_m[\mathrm{eV}] \approx 4.9(\lambda[\mu\mathrm{m}])^2\, I[\mathrm{GW/cm^2}]. \qquad \mathbf{(5)}$$

As the ionization threshold of the neutral species (Si, O, SiO and O_2) is about 12 eV, the intensity threshold at 1064 nm is about 2.2 GW/cm² and is easily reached in the experiments presented in this study.

In order to interpret the experimental results shown in Fig. 9 and quantify the axisymmetric two-dimensional mechanism described above, we estimate the velocity of the surface breakdown. This estimation is made along the x axis, parallel to the surface, which is attributed to an infinitesimal portion of the radius of a ring at the vicinity of the activation front between zone 1 and zone 2 in Fig. 12. Thus, we consider a one dimensional model which is representative of the physical process of propagation of the activation front. For that purpose, we consider that the silica surface is activated once the electron temperature in the vicinity of the surface has reached a threshold value. The heated area expands by thermal conduction mainly due to free electrons. Since the expansion velocity is much larger than estimated hydrodynamic velocities related to heavy species, their motion can be neglected as long as quasi neutrality of the medium is conserved. Thus, as we are interested in the fast mechanisms, the energy balance equation of electrons reduces to the heat equation given by

$$C_e \frac{\partial T_e}{\partial t} = \frac{\partial}{\partial x}\left(\kappa_e \frac{\partial T_e}{\partial x} \right) + \alpha I \,, \tag{6}$$

where C_e is the electron specific heat, κ_e the electron thermal conductivity and α the absorptivity. For simplicity, in this energy balance relation several processes have been disregarded, such as electron energy exchange with heavy species or screening of the laser by free electrons and hot silica. We have to keep in mind that these approximations may lead to overestimate the breakdown wave velocity. Looking for a solitary wave as a solution of the heat equation (1), it comes

$$V_a\, C_e \frac{\partial T_e}{\partial s} + \frac{\partial}{\partial s}\left(\kappa_e \frac{\partial T_e}{\partial s} \right) + \alpha(s)\, I(s) = 0 \,, \tag{7}$$

where V_a is the velocity of the activation front and s the space variable in the propagation frame defined by $s = x - V_a t$. The $s = 0$ coordinate corresponds to the border of the plasma region in Fig.12. Then, if we consider a wave traveling towards $s > 0$ (noted $^+$), absorptivity is assumed to verify $\alpha(s > 0) = 0$ and to take a constant value for $s \leq 0$ (noted $^-$). Assuming also C_e to be constant and that κ_e can take two different values, $\kappa_e^-(s \leq 0)$ and $\kappa_e^+(s > 0)$, the solution reads

$$T_e(s) = T_0 - \frac{\alpha I}{V_a C_e} s \text{, for } s \leq 0 \text{, and } T_e(s) = T_0 \exp(-\frac{V_a}{D_e^+} s) \text{, for } s \geq 0,$$

where T_0 is the threshold temperature and $D_e^{\pm} = \kappa_e^{\pm} / C_e$ the electron diffusivity. The conservation of heat fluxes through the boundary between hot and warm regions ($s = 0$) allows us to determine the velocity given by

$$V_a = \sqrt{\frac{D_e^- \alpha I}{C_e T_0}} \,. \tag{8}$$

The dielectric function of the hot region, where a free electron population of density n_e is present, can be described with the help of the Drude model. Hence, the following absorption coefficient is obtained:

$$\alpha \approx \frac{n_e e^2}{\varepsilon_0 m_e \left(\omega^2 + \nu_{ei}^2 \right)} \frac{\nu_{ei}}{n_m c} \,, \tag{9}$$

where e is the electron charge, m_e the electron mass, ε_0 the vacuum permittivity, c the speed of light, ω the laser angular frequency, n_m the optical index of the medium and ν_{ei} the electron-ion collision frequency. Two other parameters are required to define completely the activation velocity. The first one is the electron diffusivity in the hot region

$$D_e^- = \frac{k_B T_e}{m_e \nu}, \tag{10}$$

where k_B is the Boltzmann's constant, and $\nu = \nu_{ei} + \nu_{ee}$ (ν_{ee} is the electron-electron collision frequency). The second parameter is the specific heat C_e which will be assumed to be the one of a perfect gas:

$$C_e = \frac{3}{2} k_B n_e .$$

With the help of the three previous formulas, the velocity V_a is finally given by

$$V_a = \frac{e}{m_e} \sqrt{\frac{2}{3} \frac{I}{n_m \varepsilon_0 c \left(\omega^2 + \nu_{ei}^2\right)\left(1 + \nu_{ee} / \nu_{ei}\right)}}, \tag{11}$$

and shows a very low dependency with respect to the set of parameters involved in the definition of plasma state, since the collision frequency can only be much lower than ω and the optical index close to 1. Numerically, for a laser wavelength of 1064 nm $(\omega = 1.79 \times 10^{15}\ \mathrm{s}^{-1})$, neglecting ν_{ei}^2 with respect to ω^2, taking $n_m \approx 1$ and $\nu_{ee}/\nu_{ei} \approx 2$, the above formula becomes

$$V_a[\mathrm{km/s}] \approx 2.83\sqrt{I[\mathrm{GW/cm^2}]}.$$

This approach reproduces well the $I^{1/2}$ scaling law of the experimental results and gives a quantification of the thermal wave speed. It must be noted that the calculated speed remains much lower than the ones found in air environment.

V COMPARISON OF VACUUM AND AIR ENVIRONMENTS

In order to quantify the influence of the environment on the mechanisms responsible for the printing of the ring pattern, the experimental measurements obtained in vacuum and in air are reported in Fig. 13. For each configuration, twelve different ring patterns are correlated with their corresponding temporal profile to measure the evolution of the speed as a function of short-time-average intensity. Each result is fitted with a power law which exponent is set to 1/3 in air and 1/2 in vacuum. In Fig. 13, only minima and maxima fits are displayed. The small difference between minimum and maximum confirms the repeatability of the experiments. The mean values of the remaining fitting parameters are 2.75 in vacuum and 9.3 in air and are representative of the different physical processes involved in the formation of the ring pattern in both environments. We note that the absence of air reduces significantly the measured speed. In air, the propagation of an ionization front is fast enough to outdo the mechanism occurring in vacuum and silica surface is no longer the support of the activation front.

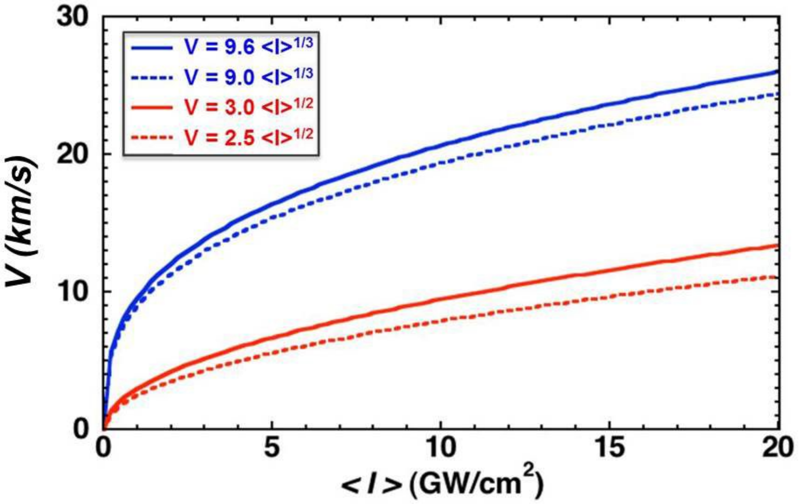

Fig. 13. Maximum (solid line) and minimum (dashed line) ring appearance speed as a function of the short-time-average intensity for both environments, air (blue) and vacuum (red).

The use of MLM pulses provides a powerful tool to investigate the chronology of events occurring during the formation of LID at 1064 nm. Indeed, the activation front starting time t_0 can be determined for each damage ring pattern. Thus, two damage formation phases can be distinguished. The first phase corresponds to the incubation of the laser flux by a subsurface defect until t_0. The second is related to the damage expansion that only refers to the energy deposit feeding the activation mechanism up to the end of the pulse. Thus, the total fluence F_{tot} of a laser pulse can be written as:

$$F_{tot} = F_{abs} + F_{exp} = \int_0^{t_0} I(t')dt' + \int_{t_0}^{+\infty} I(t')dt', \qquad \textbf{(12)}$$

where F_{abs} and F_{exp} are relative to the absorption by the precursor defect and the expansion of the ring pattern respectively. The damage diameters obtained in vacuum are thus displayed in Fig. **14** as a function of F_{tot} and F_{exp} with the ones previously obtained in air. These results suggest that there is no correlation between the size of a damage site and the fluence F_{tot} of the pulse whatever the environment. The distribution of the diameters, related to the wide range of t_0, is supposed to arise from the randomness of the precursor characteristics (absorptivity, depth, size). However, the striking feature is that the diameters are proportional to the fluence of expansion. For a given F_{tot}, if we approximate that $I(t) \approx I_{avg}$ in equation (12), we can estimate the final diameter of the ring pattern at the end of the pulse. On the one hand, equation (12) becomes:

$$F_{tot} = \Delta t_{tot} I_{avg} = \Delta t_{abs} I_{avg} + \Delta t_{exp} I_{avg}, \qquad \textbf{(13)}$$

where $\Delta t_{tot} = 9$ ns is the pulse duration, defined as the equivalent duration of the SLM pulses, Δt_{abs} refers to the duration of absorption of a precursor defect up to t_0 and Δt_{exp} stands for the expansion duration. On the other hand, the ring appearance speed is given by $v = aI_{avg}{}^{b}$, where a and b are fitting parameters. Finally, the diameter Φ of a ring pattern can be calculated as:

$$\Phi = 2v\Delta t_{exp} = 2a\left(\frac{\Delta t_{tot}}{F_{tot}}\right)^{1\ \ b} F_{exp}\,. \qquad \textbf{(14)}$$

As a consequence, the outer diameters are directly proportional to the fluence of expansion at a given F_{tot}. All the experimental values of the parameters for both air and vacuum environments are reported in Table 1. In order to show the good reliability of equation (14), two sets of data are reported for the experiments performed in vacuum that correspond to two different predetermined control fluences.

	a $(\mathrm{km.cm}^{2b}.\mathrm{GW}^{-b}.\mathrm{s}^{-1})$	b	F_{tot} $(\mathrm{J/cm}^2)$	$2a\left(\frac{\Delta t_{tot}}{F_{tot}}\right)^{1-b}$ $(\mu\mathrm{m.cm}^2/\mathrm{J})$
Air	9.3	1/3	88.5	4.05
Vacuum	2.75	1/2	63	2.08
Vacuum	2.75	1/2	103	1.63

Table 1 : Experimental values of the different parameters for both air and vacuum environments.

In Fig. 14, the coefficients of Table 1 are used to plot the lines which permit us to compare the predictions of equation (14) with experiments. The results of the two single-shot series allow us to observe the dependence of the slope of the calculated straight line with F_{tot} (cf. equation (14)) for a vacuum environment. The good agreement obtained for the three sets of experimental data justifies the approximation $I(t) \approx I_{avg}$. Moreover, equation (14) is shown to be reliable for the determination of the final diameter as a function of F_{exp} in both environments. As suggested in Fig. 7, the diameters are larger in air than in vacuum by a factor of ≥ 2 for a given F_{exp}. This observation is consistent with the different interpretations of the ring pattern formation in each environment. In vacuum, the ring pattern is clearly more concentrated than in air environment. Moreover, for a predetermined control fluence, the variation of F_{tot} around the mean value (triangles) induces a small variation of F_{exp} (circles) because of the power 1-b in equation (14) that decreases the influence of experimental scatter. However, in vacuum, when F_{tot} varies from 103 J/cm² to 63 J/cm², the slope of the calculated lines increases. This means that the incubation time Δt_{abs} is changing with F_{tot} while the expansion phase cannot last longer than Δt_{tot}. This induces a shift of the lines from right to left with decreasing F_{tot}. As a consequence of this analysis, we show that it is possible to determine F_{exp} only from the diameter of the ring pattern. Then, F_{abs} can be directly determined from the knowledge of F_{tot}. Hence, this approach can provide information on the precursor reactiveness.

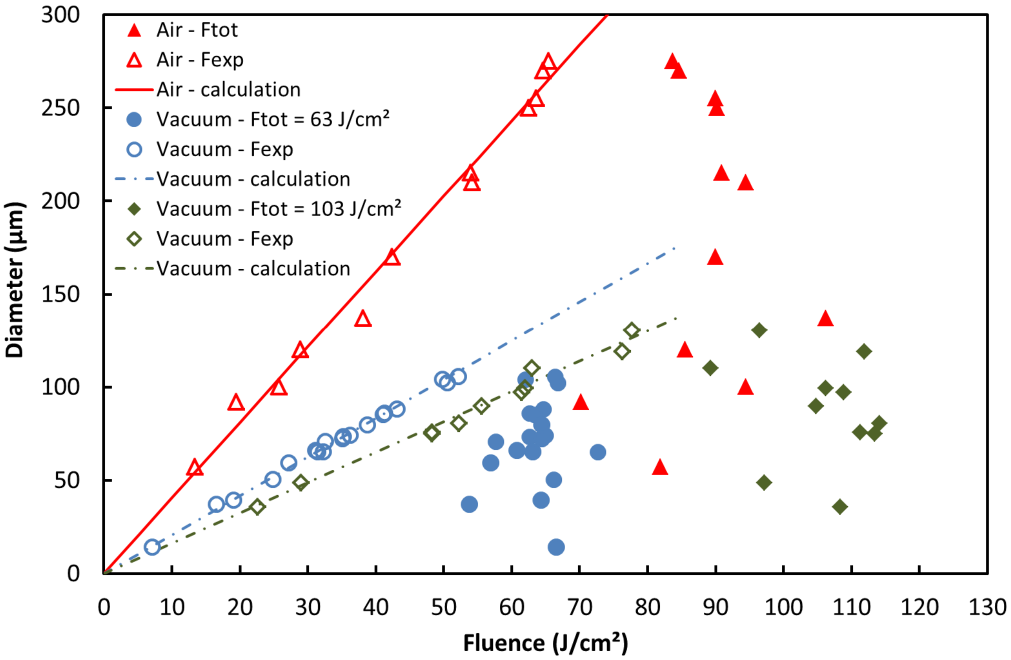

Fig. 14. Ring pattern diameters as function of total fluence (full red triangles for air and full blue circles and green squares for vacuum) and as a function of expansion fluence (empty red triangles for air and empty blue circles and green squares for vacuum). The lines correspond to the value of Table 1 calculated with the equation (14).

VI. CONCLUSION

Investigations of LID on the exit surface of synthetic fused silica at 1064 nm have been carried out with nanosecond MLM pulses. In this configuration, a ring pattern is systematically observed around the damage sites. Coupling post mortem observations to accurate laser metrology offers a powerful tool. In particular, matching the intensity spikes with the ring pattern has enabled us to precisely determine the initiation time t_0 corresponding to damage expansion beginning. During an incubation phase, before t_0, precursor defect provides energy deposit driving the near surface material up to plasma state. The time t_0 has then been determined on several damage sites, revealing a strong disparity. This result is attributed to the wide variety of precursor defects. Consequently, the final sizes of the damage sites cannot be directly correlated with the total fluence of the laser pulses. However, their sizes are proportional to the expansion fluence, calculated thanks to the precise determination of t_0.

REFERENCES

1. ISO Standard Nos. 21254-1–21254-4 (2011).
2. R. Diaz, R. Courchinoux, J. Luce, C. Rouyer, J.L. Rullier, J.Y. Natoli, and L. Lamaignère, “Experimental evidence of temporal and spatial incoherencies of Qswitched Nd:YAG nanosecond laser pulses”, Appl. Phys. B **121**, 439 (2015).
3. J.Y. Natoli, L. Gallais, H. Akhouayri, and C. Amra, “Laser-induced damage of materials in bulk, thin-film, and liquid forms”, Applied Optics **41**, 3156 (2002).
4. L. Lamaignère, T. Donval, M. Loiseau, J.C. Poncetta, G. Raze, C. Meslin, B. Bertussi and H. Bercegol, ”Accurate measurements of laser-induced bulk damage density,“ Meas. Sci. Technol. **20**, 095701 (2009).

5. L. Lamaignère, S. Bouillet, R. Courchinoux, T. Donval, M. Josse, J.C. Poncetta and H. Bercegol, ”An accurate, repeatable, and well characterized measurement of laser damage density of optical materials,” Rev. Sci. Instr. **78**, 103105 (2007).
6. G. Bataviciute, M. Sciuka, and A. Melninkaitis, “Direct comparison of defect ensembles extracted from damage probability and raster scan measurements”, J. Appl. Phys. **118**, 105306 (2015).
7. M. Chambonneau, P. Grua, J.-L. Rullier, J.-Y. Natoli, and L. Lamaignère, “Parametric study of the damage ring pattern in fused silica induced by multiple longitudinal modes laser pulses”, J. of Appl . Phys. **117**, 103101 (2015).
8. R. Diaz, M. Chambonneau, R. Courchinoux, P. Grua, J. Luce, J.-L. Rullier, J.-Y. Natoli, and L. Lamaignère, “Influence of longitudinal mode beating on laser-induced damage in fused silica”, Optics Lett. **39**, 674 (2014).
9. R. Diaz, M. Chambonneau, P. Grua, J.L. Rullier, J.Y. Natoli, and L. Lamaignère, “Influence of vacuum on nanosecond laser-induced surface damage morphology in fused silica at 1064 nm”, Appl. Surf. Science **362**, 290 (2016).
10. S. Papernov and A. W. Schmid, “Two mechanisms of crater formation in ultraviolet-pulsed-laser irradiated SiO_2 thin films with artificial defects”, J. Appl. Phys. **97**, 114906 (2005).
11. J.O. Porteus, and C. Seitel, “Absolute onset of optical surface damage using distributed defect ensembles”, Applied Optics **23**, 3796 (1984).
12. P. Combis, F. Bonneau,, G. Daval, L. Lamaignere, "Laser-induced damage simulations of absorbing materials under pulsed IR irradiation," *Proc. SPIE* **3902**, 317 (2000).
13. M. Chambonneau, R. Diaz, P. Grua, J.-L. Rullier, G. Duchateau, J.-Y. Natoli, and L. Lamaignère, “Origin of the damage ring pattern in fused silica induced by multiple longitudinal modes laser pulses”, Appl. Phys. Lett. **104**, 021121 (2014).
14. P. Grua, D. Hébert, L. Lamaignère, and J.-L. Rullier, “Role of suprathermal electrons during nanosecond laser energy deposit in fused silica”, Appl. Phys. Lett **105**, 081902 (2014).